1.0 Introduction

1.1 Background

"Soot" and "smoke" are both names for carbonaceous particulate products of fuel rich combustion. The only distinction between them is that "soot" is normally used to describe particles that are still in the flame and "smoke" refers to particles that escape the flame. Sooting flames are readily identified by their yellow-orange luminosity caused by blackbody radiation from the hot soot particles in the flame. Kerosene combustion stabilized on the wick of an oil lamp is a good example of a sooting flame, evident by its luminosity, but typically not a smoking flame because with careful adjustment of the wick height and air draught most of the particles can be oxidized before leaving the flame.

Careful control of soot formation and destruction processes is important to most practical hydrocarbon combustion systems. Regardless of whether or not soot is a desirable substance inside a combustion system, its release into the air in the form of smoke is always undesirable because of its known carcinogenic and mutagenic effects in animals and humans [Lahaye and Prado, 1983]. These health hazards of soot have prompted government intervention resulting in regulations which limit particulate emissions from industrial combustion systems. The emergence of clean air regulations and

their associated financial consequences for industry have prompted accelerated interest in understanding soot chemistry in combustion systems.

Broadband blackbody radiation from soot particles in fuel rich flames constitutes the vast majority of the combustion product's radiant emissivity in a sooting flame [Tien and Lee, 1982]. Soot's high radiant emissivity is advantageous in combustion devices such as utility boilers where heat transfer from the combustion products into some working fluid is desirable. But as mentioned previously emission of soot particles into the air as smoke is always undesirable requiring that the particles be oxidized as much as possible before leaving the device.

Production of any soot inside gas turbines and reciprocating internal combustion engines is undesirable. The design operating temperatures of many of the components in contact with the combustion products in such devices are already near their material limit and enhanced heat transfer from soot can cause reduced component life or catastrophic failure. In addition soot particles suspended the combustion products of gas turbines can cause reduced component life through mechanical erosion. Soot in the exhaust stream of military aircraft engines is disadvantageous because it can drastically compromise the stealth of the aircraft by enhancing its infrared signature.

Soot chemistry is also of great interest to understanding and controlling fires. Much of the heat transfer promoting flame spread in building and forest fires is attributable to the enhanced radiant emissivity of soot particles in the flames [Tien and Lee, 1982].

1.2 Objective

Many important combustion processes and commercial combustion devices operate neither in a purely premixed mode nor an exclusively diffusion controlled mode but rather a combination of the two. For instance in liquid fuel spray combustion some of the liquid fuel will vaporize early in the presence of air and burn in a premixed mode with the balance of the fuel burning in a diffusion limited mode surrounded by a stream of combustion products. In a discussion of the limiting cases of the premixed and nonpremixed idealisms of combustion processes Talley [1990] made the observation

> "Between these two extremes, an entire spectrum exists in which the reactants are neither completely premixed nor fully separated prior to combustion. Such situations can arise, for example, in the dropwise propagation of flames through sprays, in the propagation of flames over volatile liquid fuel surfaces, at the leading edge of lifted turbulent diffusion flames, and in many practical applications. Compared with the two better-known limiting cases, these intermediate mixtures have so far received relatively little attention."

The objective of this work was to experimentally simulate this interaction between premixed and nonpremixed combustion and study its effect on soot formation in the nonpremixed flame. The coexistence of premixed flames and nonpremixed flames will be referred to as "dual mode" combustion in the remainder of this document.

2.0 Literature Review and Approach

2.1 Overview of Soot Formation in Flames

The following discussion is not intended to be a comprehensive review of all soot formation literature (an unwieldy task indeed) but rather to provide a survey of the most widely accepted theories and conclusions as a foundation for discussions in this document. For further information the interested reader is referred to the review articles of Glassman [1988], Kent and Wagner [1984a], Calcote [1981], Haynes and Wagner [1981], Smith [1981], Wagner [1979], and Lahaye and Prado [1978].

2.1.1 Soot Particle Evolution

Five processes fundamental to soot evolution in flames are:

1. formation of molecular precursors to soot particles
2. particle nucleation or inception
3. surface growth of particles by gas phase addition
4. aggregation or conglomeration of particles
5. molecular and particle oxidation

Although these basic steps are widely accepted in the combustion community the sub-processes of each are often topics of spirited debate, especially with respect to ranking the importance of various soot particle precursors.

Soot precursor molecules are formed in hot fuel rich regions of flames favoring pyrolysis, the process of fuel breaking down into simpler molecules by thermal decomposition. Pyrolysis of ethylene (C_2H_4), used as the fuel for much of the soot research to date, yields large concentrations of acetylene (C_2H_2) which can recombine through vinylacetylene to form large molecules with an aromatic ring structure.

Regardless of the fuel and the specific mechanism of aromatic ring formation, conglomerations of these heavy aromatics known as Polycyclic Aromatic Hydrocarbons (PAH) are commonly accepted as the fundamental building blocks of soot particle nuclei [Glassman, 1988]. While these aromatic ring structures are relatively stable their constituent hydrocarbon fragments are not and are subject to competing oxidation processes during formation of the rings, thus the need for a fuel rich atmosphere to form soot.

Research on soot particle inception [Calcote, 1981, Dasch, 1985 and Glassman, 1988] revealed that the formation of the first one or two rings of a PAH is a slow process and is in fact the overall soot formation rate limiting process. Gas phase addition to these PAHs proceeds very rapidly leading to the inception of a solid soot particle. The exact dividing line between large *molecules* and incipient soot *particles* is unclear. Light scattering techniques used for estimating soot *particle* size is limited to diameters on the order of 10 nm [Kent and Wagner, 1981 and Santoro, *et al.*, 1983]. McEnally *et al.*

[1997] discuss large PAH *molecules* on the order of 1000 AMU with a corresponding diameter of approximately 1 nm. It is reasonable to bound the size distinction between molecular soot precursors and actual soot particles to lie somewhere between 1 nm and 10 nm.

Soot particles continue to grow very rapidly after inception by gas phase addition as a function of temperature, local chemical species, particle surface area and particle hydrogen content [Glassman, 1988 and Dasch, 1985]. Surface growth reactions remove hydrogen from the particles and subsequently reduce their reactivity. It is important to note that surface growth rates can be negative meaning that oxidation of carbon from the surface of a soot particle is occurring faster than addition to the surface. The relative rates of oxidation versus particle growth determines whether or not a sooting flame emits smoke [Kent and Wagner, 1984a].

Particles also grow by conglomeration and agglomeration of multiple particles at the cost of particle number density. Conglomeration refers to multiple spherical particles joining to form a larger spherical particle whereas agglomeration is the joining of spherical particles into chains.

2.1.2 Parameters Affecting Soot Formation in Flames

2.1.2.1 Temperature

The effect of temperature on the sooting tendencies of flames depends on the type of flame in question. In premixed flames fuel pyrolysis occurs in the presence of high oxygen concentrations where in nonpremixed flames there are typically negligible

concentrations of oxygen on the fuel side of the flame. Millikan [1962] showed that the rates of pyrolysis and soot precursor oxidation both increase with temperature in a premixed flame but that oxidation rates increased more quickly. As a result raising the temperature of a premixed flame lowers its sooting propensity.

By controlling the temperature of axisymmetric nonpremixed flames in air by inert dilution of the fuel Glassman and Yaccarino [1981] showed that higher temperature diffusion flames had lower smoking heights indicating a stronger propensity to soot. Kent and Wagner [1984b] similarly reported increasing laser extinction integrated soot volume fractions with increasing flame temperature. Wey *et al.* [1984b] measured increases in laser extinction soot volume fraction with increasing flame temperature for coflowing nonpremixed flames where the flame temperature was controlled by inert dilution of the oxidizer. Since the pyrolysis processes in these flames proceed virtually devoid of oxygen increases in flame temperature merely accelerate pyrolysis without the competing oxidation reactions observed in premixed flames.

Independent of the fuel used, nonpremixed flames all appear to exhibit the onset of soot particle inception at temperatures near 1400 K [Glassman, 1988]. Kent and Wagner [1984a] discovered 1300 K to be an approximate minimum temperature which supports soot particle oxidation in later regions of coflowing flames. These threshold temperature dependencies suggest activation energies associated with soot particle nucleation and oxidation. Wolfhard and Parker [1952] noted that even heating pure fuel with no oxidizer present to temperatures in excess of 1300 K can produce soot strictly by pyrolysis.

2.1.2.2 Oxygen Addition to Nonpremixed Flame Fuel

Wey *et al.* [1984b] studied the effect of adding small amounts of oxygen to the fuel stream (propane) of a coflowing Wolfhard-Parker slot burner. They found that adding oxygen to the fuel stream increased soot loading. They believed that the increases in soot loading observed was more than could be explained by thermal effects and went on to speculate that the oxygen was acting as a homogeneous catalyst accelerating fuel pyrolysis. A similar study by Hura and Glassman [1988] complemented the results of Wey *et al.* [1984b] in an axisymmetric nonpremixed flame burner and a counterflow diffusion flame stabilized on a porous ceramic cylinder. The most important conclusions of these studies is that small amounts of oxygen, on the order that will typically diffuse from the oxidizer stream into the fuel stream of nonpremixed coflowing flames, tend to increase the soot loading in those flames.

2.1.2.3 Varying Nonpremixed Flame Oxidizer Oxygen Index

The oxygen index is defined as the mole fraction of oxygen in the oxidizer stream of a nonpremixed flame. Wey *et al.* [1984a] varied the oxidizer index of Wolfhard-Parker coflowing slot burner nonpremixed flames in order to study effects of flame temperature. They considered oxygen indexes of 0.21, 0.24 and 0.29 with corresponding flame temperatures of 1973 K, 2063 K and 2195 K and peak soot volume fractions of 1.5 ppm, 2.6 ppm and 4.0 ppm respectively. They attributed the increase in soot volume fraction (soot loading) with increasing oxidizer index to strictly thermal effects.

Vandsburger *et al.* [1984] performed a similar study on counterflow diffusion flames stabilized on a porous ceramic cylinder considering oxidizer indexes from 0.18 to 0.28 resulting in flame temperatures from 1750 K to 2100 K respectively. The thermal effect of increased pyrolysis with increasing temperature in these flames resulted in peak soot volume fractions increasing from 0.2 ppm to nearly 1.0 ppm.

2.1.2.4 Radical Diffusion in Nonpremixed Flames

Diffusion of radicals from the flame front into the fuel rich pyrolysis regions of nonpremixed flames has a significant effect on the resulting soot loading [Glassman, 1988]. Most radicals, particularly atomic hydrogen, diffusing from the flame front toward the fuel side accelerate pyrolysis by initiating chain branching reactions that would not have happened otherwise.

Hydroxyl (OH) radicals are well known to be aggressive oxidizers of soot particles and soot particle precursors in both premixed and non-premixed flames [Haudiquert *et al.*, 1997 and Millikan, 1962], even more so than atomic or molecular oxygen [Fennimore and Jones, 1967]. Quantitative optical OH fluorescence measurements by Haudiquert *et al*. [1997] in Wolfhard-Parker coflowing slot burner nonpremixed flames reveal very high hydroxyl mole fractions near the flame front on the order of $6x10^{-3}$, well in excess of equilibrium predictions. Measurements by Zhang *et al*. [1992] in counterflow diffusion flames with oxidizers vitiated by carbon dioxide (CO_2) and water vapor (H_2O) revealed reductions in soot loading attributed to elevated hydroxyl concentrations at the flame front diffusing into the fuel pyrolysis region.

Soot measurements in laminar nonpremixed vaporized water / oil emulsions of various water concentrations by Rao and Bardon [1984] revealed that soot concentrations decrease with increasing water concentration in the emulsion. This reduction is partially attributed to thermal effects of the water vapor acting as a heat sink reducing flame temperatures but also a presumed increase in hydroxyl concentrations resulting from water dissociation as the reaction, $H_2O \rightarrow OH + H$, becomes favored by the high temperatures of the flame front.

2.1.3 Previous Studies on Dual Mode Combustion

Barr and Mullins [1950] performed a very thorough five part investigation of nonpremixed flames burning in vitiated air. Their motivation was to quantify the effects of exhaust gas recirculation on flame lengths, ignition and stability in aeronautical and industrial gas turbine combustors. A Burke-Schumann analysis [Burke and Schumann, 1928] of axisymmetric flames with vitiated oxidizer was followed by validating laboratory experiments and full scale gas turbine combustor tests.

Spectroscopic measurements in the laboratory scale Burke-Schumann nonpremixed flame revealed that

> "At atmospheric pressure, vitiation causes the appearance of OH bands, strengthens the CH and C_2 bands and weakens or eliminates the continuum in the region of 6,000 Å ".

where the continuum radiation is broadband radiation from soot. Barr and Mullins [1950] did not make any conclusions on soot formation from their work but it is not unreasonable to interpret their observations as water vapor in the vitiated oxidizers increasing hydroxyl concentrations at the flame front which oxidize soot precursors and reduce the soot loading.

No oxidizer or flame temperature measurements were made, making it difficult to make solid conclusions on the effect of dual mode operation on sooting characteristics observed in the laboratory flames of Barr and Mullins [1950]. Schematics of their laboratory burner show considerable lengths of plumbing between the carbon monoxide slave burner they used to vitiate the air and the Burke-Schumann burner. Assuming this plumbing was not insulated, the slave burner combustion products were probably cooled a great deal before reaching the Burke-Schumann burner. The reduction in continuum radiation observed may have been a strictly thermal effect of the vitiated oxidizer reducing the nonpremixed flame temperature.

Wirth [1989] performed experiments on an axisymmetric burner similar to that in Barr and Mullins [1950] in attempt to quantify the effect of dual mode operation on the sooting characteristics of the nonpremixed flame. Thermocouple thermometry and laser light extinction were used to characterize the *oxidizer* temperatures and nonpremixed flame soot volume fractions. No measurements of nonpremixed flame temperatures were performed.

Instead of using a slave burner to vitiate the oxidizer, Wirth [1989] stabilized lean premixed methane (CH_4) flames on a water cooled porous bronze sinter surrounding the

nonpremixed flame fuel tube yielding vitiated oxidizer temperatures ranging from 1775 K to 1900 K, certainly higher than those used by Barr and Mullins [1950]. Wirth [1989] observed higher soot loadings with increased premixed flame stoichiometry and presumed increasing nonpremixed flame temperatures.

Equilibrium calculations showed increases in oxidizer hydroxyl concentrations with increased degree of dual mode operation and subsequent increases in water vapor mole fraction. The calculations also predict decreases in oxidizer hydroxyl concentrations with height above the burner resulting from the axial temperature drop (most likely due to air entrainment). These *oxidizer* hydroxyl concentrations give little insight as to the more important hydroxyl concentrations at the nonpremixed flame front and in the pyrolysis region. Interpretation of the soot measurements of Wirth [1989] are difficult because of a lack of nonpremixed flame temperature data.

Zhang *et al*. [1992] performed studies on a counterflow diffusion flame where the oxidizer was either diluted with the products of combustion, CO_2 and H_2O, or heated (no dilution). Careful control of the peak flame temperature at 1900 K was maintained across the entire test matrix using fine wire thermocouple thermometry. Laser light scattering and extinction was used to characterize the soot aerosol and uncooled quartz microprobe sampling was used to measure chemical species concentrations including H_2, CO_2, O_2, N_2, CH_4, CO, H_2O and light hydrocarbons. They observed that preheating the oxidizer (and fuel) led to increased soot loading due to earlier soot particle inception and longer residence times. Dilution of the oxidizer with CO_2 and H_2O were observed to reduce soot loadings which was attributed to elevated hydroxyl concentrations (neither measured nor

modeled) caused by the vitiating species. By diluting with CO_2 and H_2O individually they observed decreasing soot concentrations for both but noticed that H_2O dilution had a much greater effect than CO_2 dilution.

Aftel [1996] used a counterflow diffusion flame burner with the oxidizer supplied by the products of a lean premixed hydrogen/air/oxygen flame. Thermocouple thermometry was used to match flame temperatures across the test matrix by varying the oxidizer index. Laser light scattering and extinction and laser induced fluorescence measurements were used to characterize the soot aerosol and qualitatively indicate PAH concentrations. He observed that soot volume fractions decreased with increasing degrees of dual mode operation which was attributed to elevated hydroxyl concentrations. Soot particle diameters were observed to decrease and particle number densities were observed to increase with increasing degrees of dual mode operation. Interpretation of these observations was that the elevated OH had little effect on soot particle nucleation and that coagulation and agglomeration was much more aggressive in the single mode flames than in dual mode flames. These results are interestingly contrary with the results of other investigators [Dasch, 1985 and Glassman, 1988] which concluded that overall soot loading is primarily limited by particle inception.

2.2 Approach Chosen for the Present Study

The work of Aftel [1996] offered interesting insight into the nature of dual mode flames and their effect on sooting characteristics. It was decided to tailor the scope of this research as an extension of Aftel's work.

Counterflow diffusion flames such as the one used by Aftel [1996] offered a good simulation of the coupled fluid mechanical and combustion processes observed around liquid droplets burning in crossflow. Its one-dimensional stagnation streamline facilitated both measurements and modeling. The only considerable disadvantage of the counterflow diffusion flame was the small scale of the sooting region. The distance from the flame front to the burner cylinder was on the order of 5 - 7 mm with the sooting region spanning only 2 - 3 millimeters, placing a large premium on measurement spatial resolution.

Although coflowing nonpremixed flames have shorter soot particle residence times [Kang *et al*., 1997] they demand less stringent measurement spatial precision to effectively characterize the flames and were chosen for this study. Axisymmetric diffusion flames like those used by Wirth[1989] and Santoro *et al*. [1983] provide long, ~10 cm, steady flames but their radial symmetry requires complex tomographic reconstruction of optical line of sight measurements to extract the soot characteristics at a point. Instead, a Wolfhard-Parker coflowing slot burner geometry [Wolfhard and Parker, 1952 and Kent and Wagner, 1982] was selected for this study because its rectangular symmetry offers a nearly homogeneous line of sight path greatly simplifying optical measurement analysis. Similar to Wirth [1989] and Aftel [1996] the products of lean premixed flames were chosen as the dual mode oxidizer to simulate nonpremixed laminar flamelets burning in the wake of

previously burner fuel / oxidizer mixture often used to model turbulent nonpremixed combustion [Peters, 1986, Flower, 1988 and Moss *et al*., 1988].

2.2.1 Survey of Wolfhard-Parker Laminar Nonpremixed Flame Studies

The following discussion is organized as a chronological listing of laminar flame studies using the Wolfhard-Parker burner geometry. These publications provided insight and "hind-sight" which influenced the experimental design and scope of this study.

Wolfhard and Parker [1952] are credited with concept of using a coflowing slot burner for combustion research. Their burner consisted of one fuel slot and one oxidizer slot producing a single flame 7 cm tall and several millimeters thick. Temperatures were measured by sodium line reversal and optical absorption and emission techniques were used to measure O_2, OH, C_2, C and CH in ammonia / oxygen and ethylene / oxygen nonpremixed flames. On their spectroscopic observations in the sooting region of the ethylene / oxygen flame, just on the fuel side of the flame front, they remark

> "Water vapour, carbon dioxide and carbon monoxide are present however and diffuse from the main reaction zone. These gases may react with the carbon particles but their influence as far as pyrolysis and carbon formation are concerned is probably small and largely a dilution effect."

Haynes and Wagner [1980] used a slightly modified version of the Wolfhard-Parker burner with two oxidizer slots sandwiching the fuel slot creating two laminar flame fronts which they found promoted flame stability. Laser light scattering and extinction measurements with Rayleigh analysis was used to characterize the soot aerosol at

individual spatial locations. They concluded that the only region that thermally and chemically supports particle inception is just on the fuel side of the flame front. The particle sizes and overall soot loading were observed to increase with decreasing particle number densities as particles were convected upward through the flame to a point where the soot volume fractions began to decrease. Decreasing number densities happening simultaneously with increases in soot volume fraction were attributed to combined particle coagulation and surface growth.

Kent *et al*. [1981] extended the study of Haynes and Wagner [1980] by adding temperature measurement by thermocouple thermometry and the Kurlbaum method and velocity measurements by single component Laser Doppler Velocimetry. Using the velocity measurements combined with conservation of mass to calculate the transverse velocity components the soot measurements made in Eulerian (laboratory) coordinates were transformed into Lagrangian (particle tracking) coordinates, allowing calculation of *rates* of soot volume fraction, surface growth and particle generation. Particle generation rates were found to be a maximum several millimeters on the fuel side of the flame front and then became very small or negative as the result of particle coagulation and agglomeration. Soot volume fraction rates and particle size growth rates were both observed to increase as the particles were convected through the flame.

Kent and Wagner [1982] applied the particle tracking techniques reported in Kent *et al*. [1981] for an array of fuel and oxidizer flow rates. Refinements were made to their laser light scattering analysis by using the full Lorentz-Mie solution for light interaction with particles instead of the Rayleigh limit theory used previously. They observed that the

initial momentum of the fuel flow had little effect on the final centerline velocities concluding that the flames were predominately buoyancy driven. In fact the flames with the lowest initial momentum achieved the highest centerline velocity because of their lower thermal capacitance. The lower fuel flow rate cases peaked with very high integrated soot volume fraction fluxes and then decreased sharply. The high fuel flow rate cases showed less soot early but steadily continued to grow surpassing the soot flux of the low fuel flow rate cases. Maximum soot particle number densities with height for each of the cases were indistinguishable from one another.

Wey *et al*. [1984a] investigated the effect of flame temperature on the sooting tendencies of nonpremixed propane flames stabilized on a Wolfhard-Parker burner by varying the oxidizer index. They concluded that hotter nonpremixed flames produced more soot. They continued in Wey *et al*. [1984b] by studying the effects of oxygen addition into the nonpremixed flame fuel on soot. They concluded that the addition of small amounts of oxygen (typical of those that might diffuse into the fuel stream in coflowing flames) to the propane nonpremixed flame fuel tends to raise the sooting tendency. They added that the increase in soot loading was more than could be described by a thermal mechanism and proposed that homogeneous catalysis of pyrolysis reactions by the oxygen was likely.

Flower [1986] presented results from a study of laminar nonpremixed Wolfhard-Parker flames at elevated pressures up to 2 atmospheres. Laser Doppler Velocimetry and laser light scattering and extinction were used to measure velocities and characterize the soot aerosol. Soot volume fractions were determined to increase with pressure to the

power of 1.7 and integrated soot volume fraction fluxes were found to increase with pressure to the power of 7.0.

Smyth *et al*. [1985] made an array of optical species measurements along with Laser Doppler Velocimetry velocity measurements and Laser Light Scattering and Extinction soot aerosol characterization using a Rayleigh analysis in methane/air Wolfhard-Parker flames. They observed that species concentrations appeared to follow isotherms instead of streamlines. In their discussion of thermocouple thermometry used to measure flame temperatures they expressed concern over the great uncertainty in their knowledge of the thermocouple's Nusselt number and its profound effect on radiation corrections and kinetic interpretation of the species measurement data.

Moss *et al*. [1988] performed microprobe gas sampling, thermocouple thermometry and laser extinction soot volume fraction measurements in ethylene / air Wolfhard-Parker flames in support of a flamelet approach to modeling soot formation. Compositions of sampled gases were used to spatially map mixture fraction in the flames. Mixture fraction versus temperature data was found to collapse into a single curve for several heights in two flames at different pressures. They found that soot formation processes predominantly occur in the band of mixture fractions $0.07 \leq \zeta \leq 0.2$ where a mixture fraction of $\zeta = 0.063$ indicates stoichiometric proportions. The model was extended in Moss *et al*. [1995] to include soot oxidation where they conclude that OH was the dominant soot oxidizing species in similar Wolfhard-Parker flames consistent with Fennimore and Jones [1967].

Smyth *et al*. [1990] made quantitative hydroxyl radical concentrations in laminar methane / air Wolfhard-Parker flames. Measured values were as much as twice the equilibrium values consistent with the observations of Fennimore and Jones [1967] but less than partial equilibrium calculations would indicate. Similar observations of hydroxyl radical concentrations were made by Haudiquert *et al*. [1997] in ethylene/air Wolfhard-Parker flames.

Norton *et al.* [1993] partially repeated and extended the work of Smyth *et al*. [1985] in methane / air Wolfhard-Parker flames to include optical measurement of five combustion radicals, OH·, H atom, O atom, CH· and CH3·, and comparison of the accumulated experimental database with an axisymmetric nonpremixed flame model. Good agreement was achieved between the geometrically dissimilar model and experiment when compared in conserved scalar coordinates.

2.2.2 Measurement Techniques

Almost all past investigators of soot in Wolfhard-Parker flames deemed soot volume fraction, particle number density and particle diameter measurements by laser light scattering and extinction both necessary and sufficient to completely characterize the soot aerosol at any given point in the flame. The laser light scattering and extinction technique was therefore also adopted for this study.

A review of the literature reveals that temperature is an absolutely critical parameter with respect to soot formation in flames. Fine wire thermocouple thermometry utilizing a rapid insertion technique and radiation corrections was selected for gas temperature measurement.

Considering the two dimensional nature of Wolfhard-Parker flames Particle Imaging Velocimetry was chosen as the method for measuring gas velocities. Past studies [Kent and Wagner, 1981 and Kent and Wagner, 1982] have proven the value of comparing the sooting characteristics of flames on a flux basis rather than just local intensive properties.

3.0 Experimental Apparatus and Methods

3.1 Dual Mode Wolfhard-Parker Burner

A coflowing, rectangular slot Wolfhard-Parker burner was used for this study. The burner, shown schematically in Figure 3.1, consisted of three slots, all nominally 60 mm long and 152 mm (6 in) tall, with a 6 mm wide hydrocarbon fuel slot sandwiched between two 16 mm oxidizer slots. All slots were bounded along their East and West sides by 1.6 mm (1/16 in) stainless steel partitions tapered to a sharp edge on top with a half-angle of approximately 45°, Figure B3. All slots were bounded on their North and South sides by 3.2 mm (1/8 in) untapered stainless steel walls, Figures B1 and B2. The burner assembly, Figure 3.2, was fastened by its base, Figures B4 - B8, to an aluminum manifold, Figure B11, which supplied the test gases into the individual slots. The burner to base connection was sealed with the gasket shown in Figure B9 and the base to manifold connection was sealed with the gasket shown in Figure B10 both fabricated from 1/8 in thick neoprene.

The hydrocarbon fuel entered the base of the fuel slot through an array of 16 - 0.8 mm (1/32 in) diameter holes, Figures B4 - B8. The fuel flow was cooled by eight passes of a water cooled 1/8 in copper tube over the first 100 mm height of the fuel slot. Flow

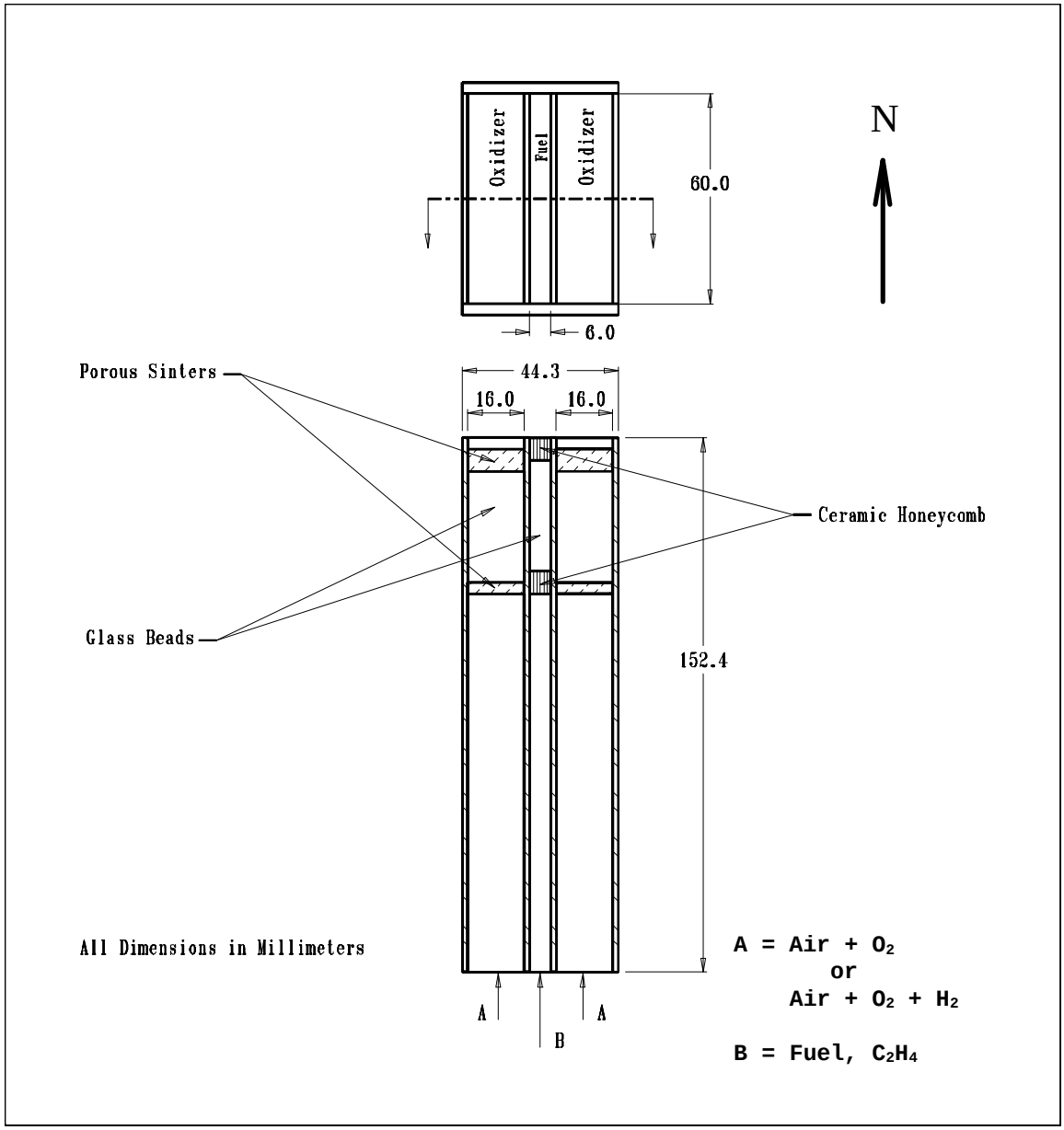

Figure 3.1 Wolfhard-Parker Burner Schematic

conditioning for the hydrocarbon fuel slot began at a height of 109 mm consisting of a 6.4 mm (1/4 in) thick, 1mm square matrix ceramic monolith, Figure 3.3, located 112 mm (4.4 in) vertically above the base of the slot followed by a screen, 30 mm thick bed of 2 mm ceramic beads, another screen and an identical square ceramic monolith whose top

edge sat flush with the upper lip of the burner. Typical residence time for the fuel in the hydrocarbon fuel slot at 3.3 cm/s nominal cold velocity was approximately 4 seconds with the first 3 seconds water cooled.

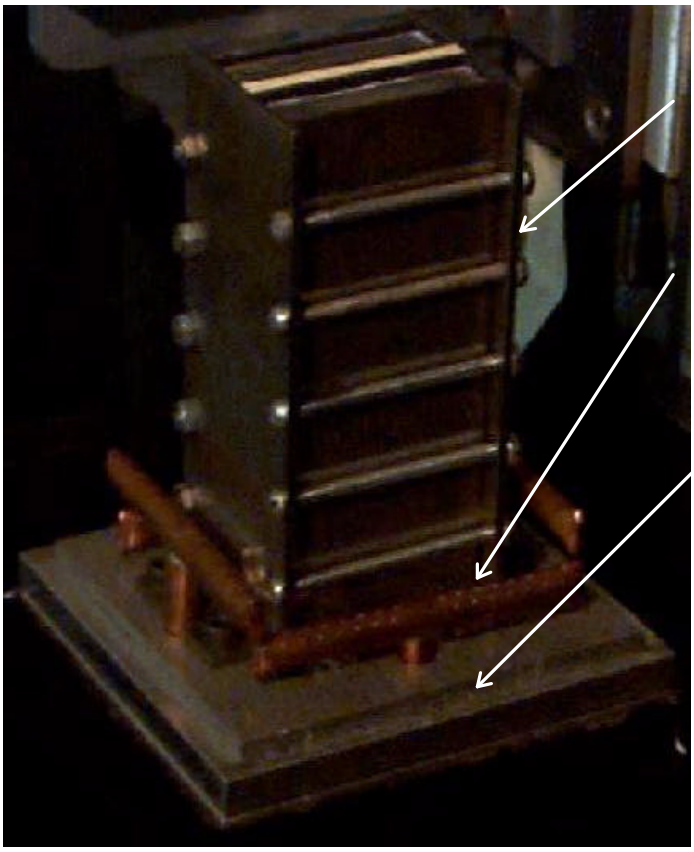

Figure 3.2 Burner / Base Assembly

An Air / Oxygen mixture entered each of the two oxidizer slots through an array of 48 - 0.8 mm (1/32 in) diameter holes in the base of the slot, Figures B4 - B8. Hydrogen for the dual mode cases was injected in counterflow to the Air/Oxygen flow through an array of 16 - 0.8 mm (1/32 in) diameter holes in a 1/4 in diameter copper tube located 10

mm above the base of the slot. The Hydrogen mixed freely with the Air/Oxygen mixture for a vertical distance of 103 mm (4.4 in) . Flow conditioning for the oxidizer slots began at a height of 113 mm with a 3.2 mm (1/8 in) thick coarse pore bronze sinter followed by a 20 mm thick bed of 3 mm diameter borosilicate glass beads and finally a 6.35 mm (1/4 in) thick, 20 μm pore Inconel sinter whose exit plane sat 3 mm below the burner slot lip. Typical residence time for the oxidizer mixture at 6 cm/s nominal cold velocity was approximately 2.5 seconds with free mixing of the Hydrogen/Oxygen/Air mixture for the first 1.7 seconds.

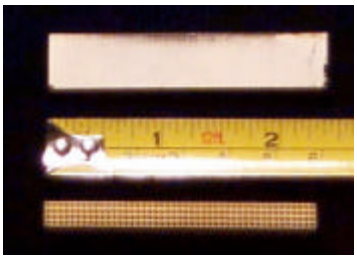

Figure 3.3 Ceramic Honeycomb Flow Conditioning

Sinters were chosen as the final flow conditioning for the oxidizer slots to uniformly stabilize the Hydrogen/Air/Oxygen premixed flames and prevent the premixed flames from flashing back into the mixing region of the oxidizer slots during dual mode operation. The 20 μm pore Inconel sinters (Mott Metallurgical Corporation, Farmington CT) were chosen because their pore dimension was much less than the quenching distance for premixed Hyrdogen/Air flames, 510 μm [Rosner, 1986], and since they were rated at 866 K (1100 °F) in oxidizing atmospheres they did not require direct cooling.

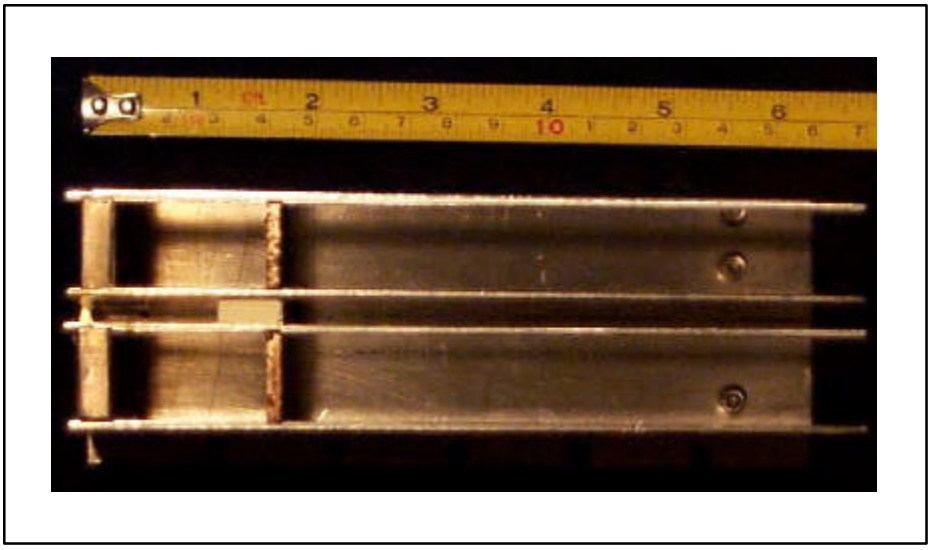

Figure 3.4 Burner Cross Section

Although the Inconel sinters' pore dimensions were well below the quenching distance the premixed flames were still observed to flash back in dual mode operation. It was speculated that even though the sinters' mechanical properties easily withstood the operating temperature they were getting hot enough on their inlet side to act as an ignition source for the mixing region inside the oxidizer slots. Water cooled heat exchangers installed on the exterior of the burner eliminated the observed premixed flame "flash backs."

The burner assembly was enclosed in a 305 mm tall, constant cross section square duct of 120 mm x 110 mm used to isolate the burner from room draughts and control overall nonpremixed flame stoichiometry, Figures B12 - B15 and Figure 3.5. Each of the duct walls had 73 mm x 124 mm (2 7/8 in x 4 7/8 in) square openings centered horizontally and beginning 2 mm below the upper burner lip vertically. Windows or aluminum panes could be installed in the openings for optical and thermocouple probe

access. Nitrogen coflow was injected 15 mm above the aluminum manifold between the burner and the enclosure. Flow conditioning for the coflow consisted of a fine mesh screen sitting 10 mm below the burner lip. Diffusion flame attachment screens were placed in the exit of the burner enclosure to promote flame stability.

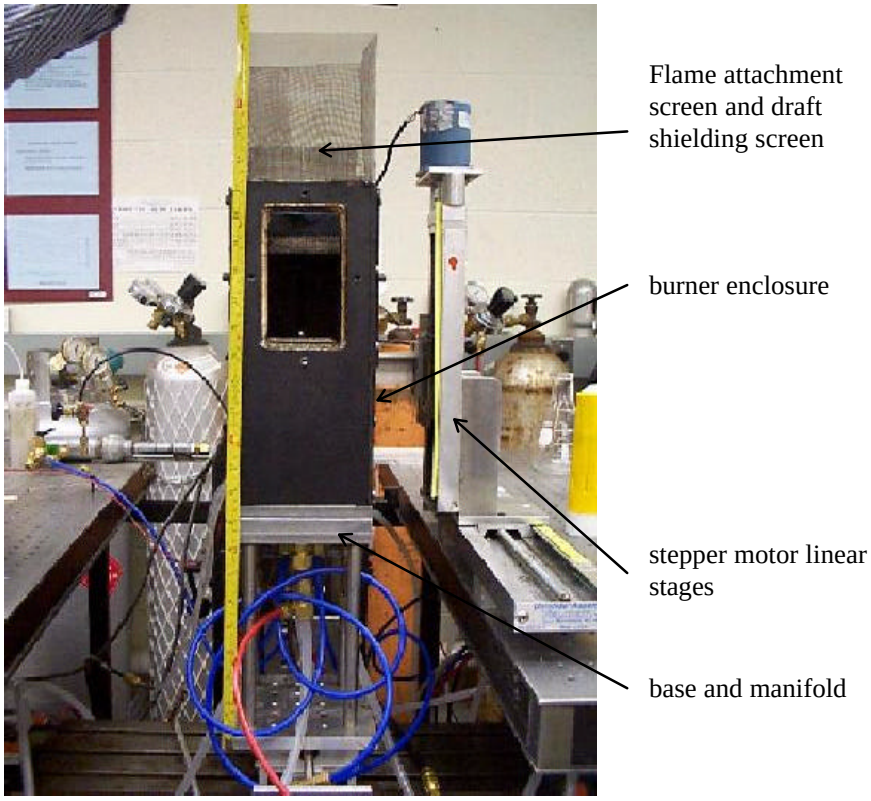

Figure 3.5 Burner Enclosure Assembly

3.2 Gas Supply and Metering

Filtered and dried air for the Wolfhard-Parker burner was supplied by a lab compressor. Commercial grade (99.0 % pure) oxygen, hydrogen, ethylene and nitrogen were supplied from 200 scf, 2000 psi gas cylinders. All gas flows into the burner manifold were metered using calibrated Mathesson rotameters. Calibration curves for rotameters

used are shown in Appendix C. A volume flow integrating dry test gas meter was used as the standard for rotameter calibrations. Static density at the inlet of the rotameters was held constant at the values reported in Appendix C during the calibrations. All volumetric flow rates reported are for the gas at standard temperature and pressure (1atm, 300 K). Flows to each of the two oxidizer slots (air, oxygen and hydrogen) were metered individually with identical rotameters in parallel.

3.3 Computer A/D Board and Stepper Motor Linear Stages

Experiments requiring data collected over an array of individual spatial locations (thermocouple thermometry, Thermocouple Particle Densitometry (TPD) and Laser Light Scattering (LLS) and Extinction (LLE)) were automated using computer controlled, stepper motor driven, linear stages and a Data Translation DT2805 A/D board to digitize analog inputs for computer data collection. Stepper motors and the A/D board were controlled via FORTRAN code executed on a personal computer. A typical two-dimensional linear stage arrangement is shown on the right of Figure 3.5. A/D board range and zero adjustments were performed using a NIST traceable Fluke precision voltage source as a reference with results shown in Figure 3.6.

All linear stage stepper motors had 200 steps per revolution. Linear stages with a screw pitch of 5 threads / in and translation precision of 25 μm / step were used for horizontal and vertical thermocouple manipulation. A horizontal linear stage with a pitch of 16 threads/in and precision of 8 μm / step was used for horizontal translation of the burner for laser light scattering and extinction measurements. Vertical translation of the

burner was accomplished manually using the 10 thread / in vertical screw of the milling machine base to which the burner was mounted.

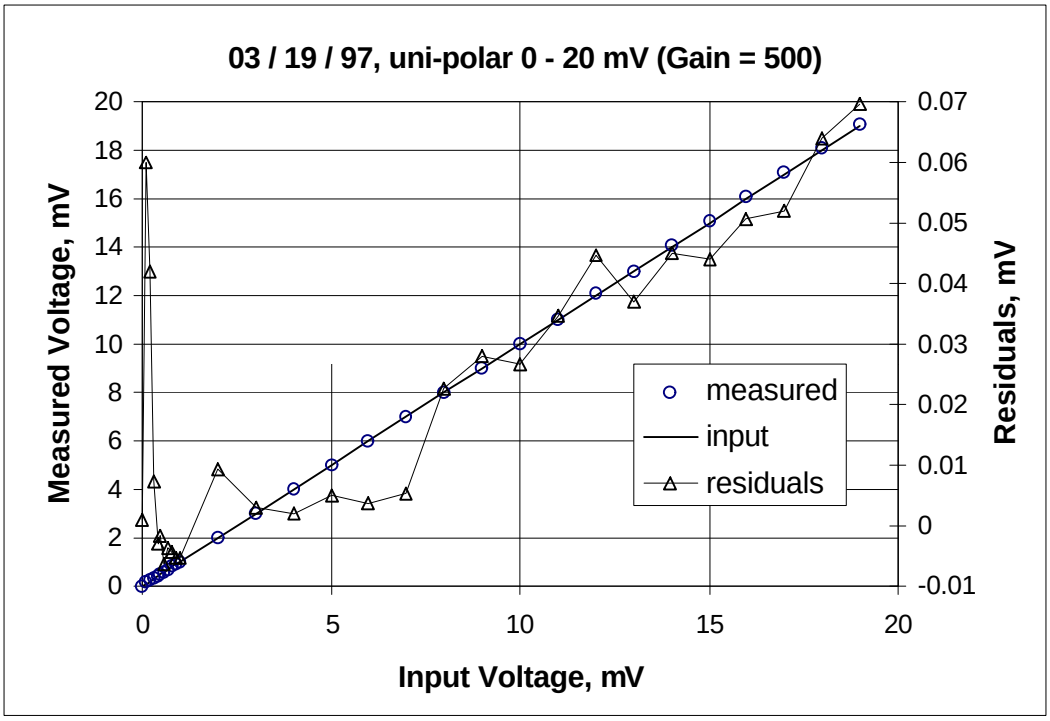

Figure 3.6 DT2805 A/D Board Calibration Results

3.4 Temperature Measurement

3.4.1 Thermocouple Construction and Preparation

50 μm diameter type-B thermocouple wire (Platinum-6%Rhodium (-) / Platinum-30% Rhodium (+)) was used to fabricate the thermocouple junctions for this study. Type-B thermocouples were chosen for their high temperature rating, up to 1820 K, and chemical stability in oxidizing atmospheres. Peak junction temperatures measured in the Wolfhard-Parker burner flames exceeded the type-B rating by as much as 30 K. Linear

extrapolation of the reported type-B thermocouple calibration data was used for junction temperature measurements in excess of the rated maximum temperature.

The junction and fine wire leads were supported by 250 μm type-B wires threaded through a 1/8 in OD x ~10 in long double bore ceramic rod (Vesuvius Incorporated) as shown in Figure 3.7. Typical junction diameters were 100 ± 15 μm approximately twice the fine wire diameter as shown in Figure 3.8. A wire diameter of 50 μm was chosen for making the junctions being the smallest available type-B wire in the lab. Smaller thermocouple wires offer better spatial resolution and less extensive viscous influence on the flow (i.e. smaller Reynolds numbers based on wire diameter). Wires of 250 μm diameter were selected for the fine wire supports on the advice of Sivo [1997] for being "small" but still rigid enough to keep the fine wires taut.

Copper/type-B(+) and copper/type-B(-) junctions have nearly identical thermoelectric potentials. As a result, ice bath cold junction compensation yields a very small adjustment to the potential across the measurement junction (~0.1 °C) [Omega Temperature Measurement Handbook] and is commonly neglected for type-B thermocouples. Choosing to neglect cold junction compensation, the type-B thermocouples used in this study were directly wired to the A/D board via uncompensated copper terminals (Omega Incorporated) and copper extension wires.

Although type-B thermocouples are relatively resistant to oxidative attack in combustion environments they are not immune to contamination and their high platinum composition favors heterogeneous catalysis on the wire's surface [Madson and Theby,

1984]. Catalysis on the thermocouple's surface tends to raise the temperature of the gas stream locally by promoting predominantly exothermic radical recombination reactions that would not have occurred without the thermocouple's presence. Catalysis on the surface of thermocouples can raise the measured junction temperature by more than 100 K in combustion environments.

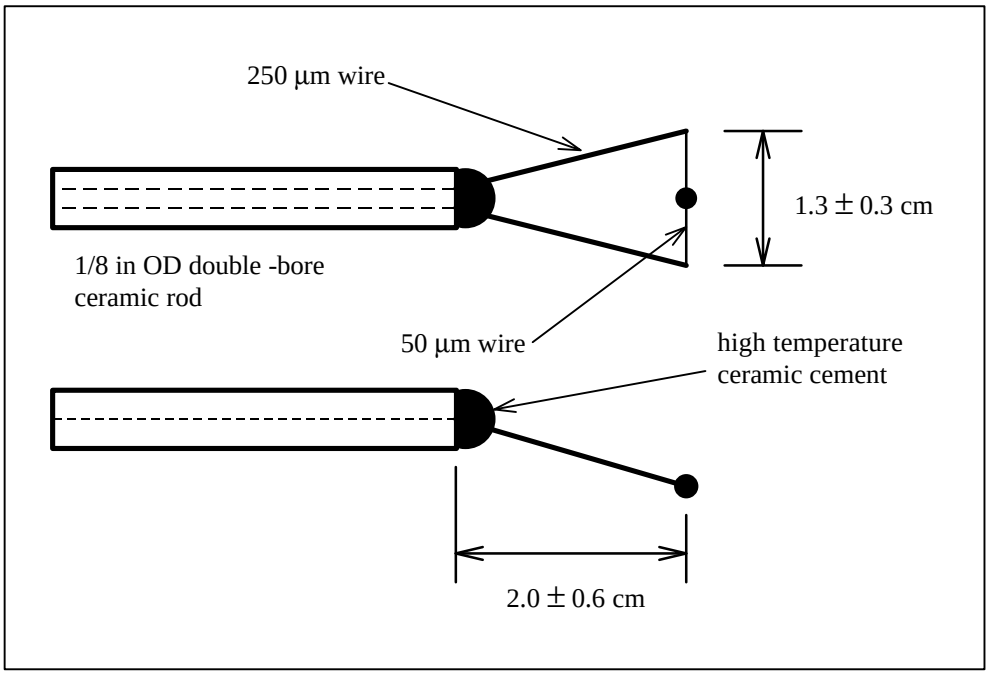

Figure 3.7 Thermocouple Construction Schematic

To prevent catalytic influences on the thermocouple thermometry measurements all thermocouples were coated with silicon dioxide (SiO_2). Thermocouples were coated by placing them in a premixed propane/air flame with hexamethyldisiloxane dissolved into the propane. In the premixed flame the hexamethyldisiloxane burns yielding SiO_2 particles which are thermophoretically (see Appendix A Section 3) driven to the thermocouple's surface where they conglomerate to form a glassy coating on the surface of the

thermocouple junction and lead wires. The thermocouple junction temperature and duration in the flame for coating were carefully monitored to ensure repeatability in coating thickness among the thermocouples prepared. Imaging microscopy of the coated junctions revealed typical coating thicknesses of 10 μm (added to radius).

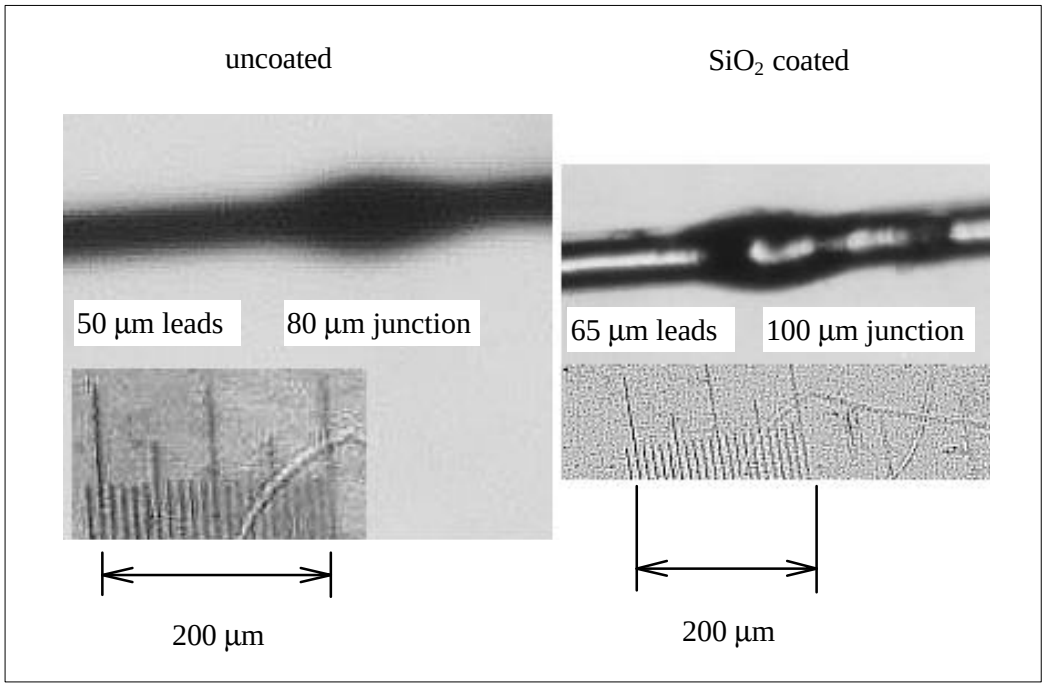

Figure 3.8 Typical Thermocouple Junction

3.4.2 Implementation of Rapid Insertion Thermocouple Thermometry and Thermocouple Particle Densitometry (TPD)

A background discussion of thermocouple thermometry in combustion environments is presented in Appendix A. Familiarity with the contents of Appendix A is assumed for this section's discussion of the details of thermocouple thermometry specific to this study.

Thermocouples were used to make temperature and TPD soot volume fraction measurements in spatial increments of 0.5 mm horizontally and 5 mm vertically. The double bore ceramic rod passed horizontally through a vertical slot in the burner enclosure with the thermocouple wire oriented parallel to the burner slots and isotherms to minimize conduction effects. Collection of data by an A/D board to a personal computer and manipulation of thermocouple location by two linear stepper motor stages were completely automated using FORTRAN routines. Voltages measured across the thermocouple junction were converted to temperatures in the software by linear interpolation of thermocouple table data in 5 K increments [ANSI MC 96.1, 1975].

Successful implementation of both thermocouple thermometry and TPD techniques require knowledge of the thermocouple's time response in the flame. In non-sooting regions of the flame the thermocouple's thermal capacitance is the only important transient behavior and thermocouple's equilibrium temperature may be measured using an average sampling technique. The average sampling technique involves traversing the thermocouple to the location of interest, pausing at least five time constants to ensure thermal equilibrium between the thermocouple junction and the gas and then averaging over an arbitrarily large number of samples.

Figure 3.9 shows a graphical representation of thermocouple time constant determination according to equation A.4. Time constants for various thermocouples were typically 0.4 ± 0.02 seconds. These thermocouples are much slower than the time constants reported for the slightly larger diameter but uncoated thermocouples used by McEnally *et. al.* [1997] of 0.1 seconds. No time constants for bare thermocouple

junctions were measured in this study for comparison but it is reasonable to attribute the slower time response on the low thermal conductivity and high heat capacity ceramic coating. It is important to note that the slower time response of the coated thermocouples used in this study was not a large disadvantage considering that the flame under investigation was steady and laminar. However it was important to accurately identify the magnitude of a typical thermocouple's time constant. For average sampling in this study data collection was delayed for 2 seconds (~5τ) to allow the thermocouple to equilibrate with its surroundings and then the average of 10,000 samples collected at 8 kHz over 1.25 seconds was reported as the thermocouple surface temperature.

As the thermocouple passes from the flame front into the sooting region of the flame the average sampling technique fails to report accurate equilibrium temperatures as a result of thermophoretic soot transport to the thermocouple's surface. To resolve an estimate of what the clean junction equilibrium temperature would have been in the absence of soot deposition a rapid insertion technique was employed in the sooting region. The temperature traces required for temperature measurement in sooting regions were additionally used as input to a Thermocouple Particle Densitometry (TPD) analysis to quantitatively determine local soot volume fractions.

A rapid insertion sampling technique requires approximately 30 seconds per sample whereas the average sampling algorithm only takes about 5 seconds per sample. When collecting samples at over 600 spatial locations with less than 25% in soot laden regions, as was the case in this study, one can readily see the time advantage of

using a combined average sampling / rapid insertion sampling temperature measurement algorithm.

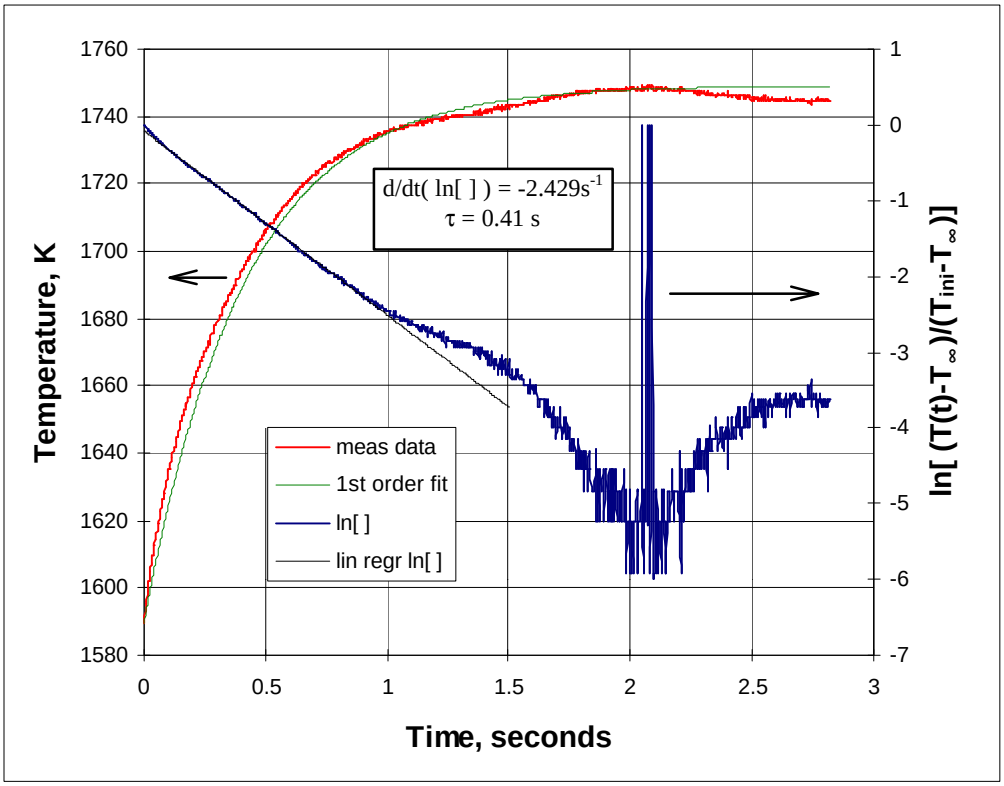

Figure 3.9 Thermocouple Time Constant, τ, Determination

Beginning with each horizontal traverse an average sampling algorithm was used until a peak temperature of 1600 K on the *oxidizer side* of the flame front was measured triggering a switch to the rapid insertion sampling algorithm. The temperature 1600 K was chosen as the trigger value because it was visually determined to be the optimum location for burning off soot between rapid insertion measurements. It is tempting to choose the maximum temperature (i.e. flame front at 1850 K) as the location for burning off the soot until one rationalizes that very little oxygen, required to burn the soot off of the thermocouple, is present at the flame front in a non-premixed flame. In the higher

regions of the flame where maximum temperatures are less than 1600 K the rapid insertion sampling algorithm was triggered by the spatial change in slope at the maximum transverse temperature and soot was burned off between samples at a lower, more oxygen rich, height in the flame whose coordinates were stored in the computer's memory earlier in the experiment. All soot burning steps in the automated algorithm were timed manually by inserting "PAUSE" statements in the code and continuing after a visual determination of the thermocouple's cleanliness was ascertained (2 to 10 seconds typical).

In the rapid insertion algorithm the thermocouple was traversed from the "cleaning" position (1600 K trigger location) to the sample location where 1000 samples were collected at 100 Hz over 10 seconds. Since the rapid insertion algorithm was triggered on the oxidizer side of the flame, possibly several millimeters away from the sooting region, the sample may have been collected in a non-sooting region as shown in Figure 3.9 or a sooting region as shown in Figure 3.10.

To correctly interpret Figure 3.10 and to compare it to the time traces published by others in the literature it is important to point out that the initial temperature before insertion was the *cleaning* temperature, 1600 K, and not ambient temperature as in Govatzidakis [1993] and McEnally *et. al*. [1997]. The first two seconds of Figure 3.10 appear to be dominated by variable emissivity effects as described in McEnally *et. al.* [1997] but are actually dominated by capacitive *cooling* from its initial temperature of 1600 K (recall that 5τ for the thermocouples used in this study is ~2 seconds).

Linearity in the transformation G(t) (from TPD analysis) shown on the right axis of Figure 3.10 indicates variable diameter behavior beginning after 2.5 seconds. Notice that

with the slower coated thermocouples used for this study distinct capacitive transient and variable emissivity regions were not observed, but rather occurred simultaneously.

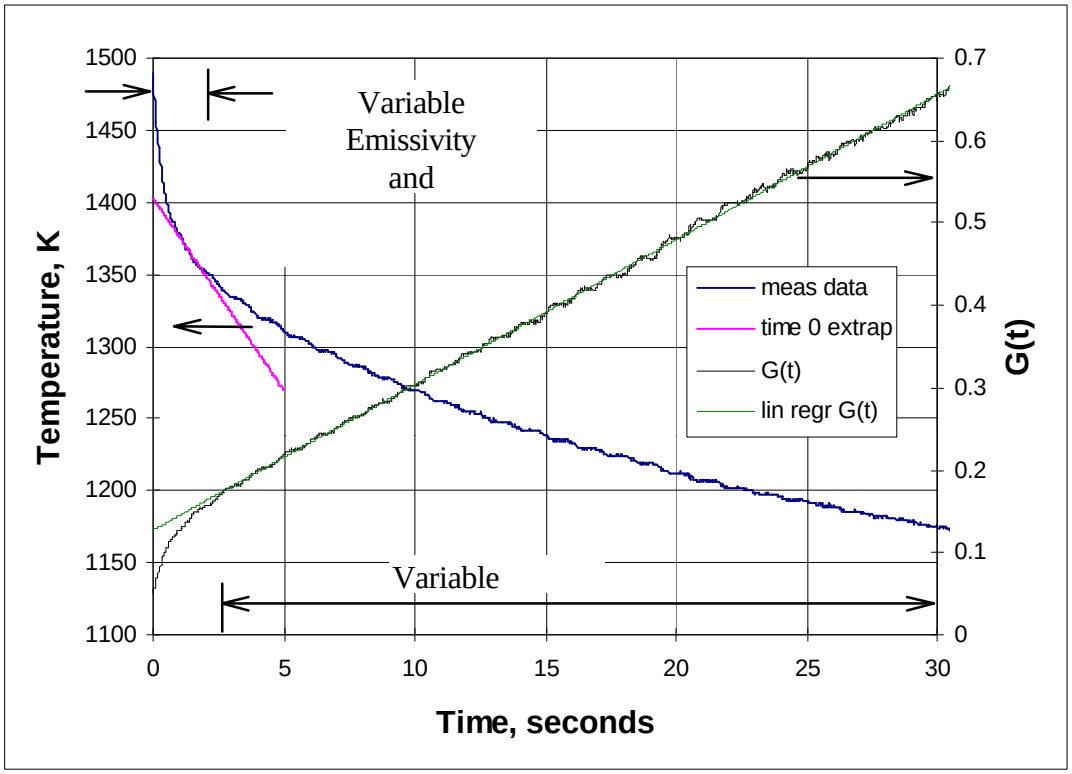

Figure 3.10 Thermocouple Temperature Versus Time in a Sooting Region

In the non-sooting time trace (Figure 3.9) the temperature versus time slope for large times is nearly zero and the slope of the temperature profile in the sooting region (Figure 3.10) is negative. The determination of whether or not soot was present during the temperature measurement was made by a linear regression of the portion of the time trace after the capacitive transient and comparing the slope to a nearly zero, negative number. Some temperature profiles in clearly non-sooting regions had slightly negative slopes because of noise in the signal so zero was not a good choice for a critical slope

value. A critical temperature versus time slope of -0.05 K/sec was found to work well in discriminating between soot affected and soot free temperature profiles.

If the slope for 5 s ≤ t ≤ 10s was greater than or equal to the critical slope, as in Figure 3.9, the thermocouple surface temperature was calculated as the average of samples taken after the capacitive transient, 2 seconds. For temperature slopes less than the critical slope the soot free thermocouple temperature was approximated using a transient analysis of the junction temperature profile with simultaneous TPD analysis.

Govatzidakis [1993], using thermocouples whose calculated time constants (not measured) were approximately 0.1 seconds, chose to linearly extrapolate the temperatures between 0.1 and 0.3 seconds to time zero (instant of insertion) as an approximation of the soot free thermocouple temperature. McEnally *et. al* [1997] using thermocouples with measured time constants of 0.2 seconds chose to average the temperatures between 0.5 and 1.0 seconds after insertion. For this study the soot free thermocouple temperature was chosen as the time zero linear extrapolation of the temperature profile for 1 s ≤ t ≤ 2s as shown in Figure 3.10. This scheme avoids extrapolation over the steepest portion of the capacitive transient region and the early portion of the variable diameter region.

The previously discussed temperature measurement methods yield good estimates of the *thermocouple* equilibrium temperature in sooting and non-sooting regions of the flame. The desired gas temperatures still have to be determined by correcting for steady heat transfer processes preventing the thermocouple surface temperature from assuming the local gas temperature. All thermocouple temperature measurements were corrected to yield gas temperatures as described in Appendix A. Nusselt numbers for the thermocouple

junctions were estimated relative to empirical relationships for cylinders and spheres (Equations A.21 and A.22) according to Appendix A.5 as

$$Nu_d = Nu_{d,\,sphere} - \eta\,(Nu_{d,sphere} - Nu_{d,\,cylinder})$$

$$\text{with} \quad \eta = \mathbf{0.9}$$

indicating primarily cylindrical convection heat transfer behavior. Values of radiant emissivity for the SiO_2 coated thermocouples versus temperature were taken from Bradley and Entwistle [1966]. All fluid properties of the combustion products were assumed to be identical to those of air at the same temperature. The velocity field used for temperature corrections was derived from Particle Imaging Velocimetry Measurements as discussed in the later section 3.6.

3.5 Laser Light Scattering and Extinction

Consistent with previous studies [e.g. Kent and Wagner, 1982, Santoro et. al., 1983 and Vandsburger, 1986] soot volume fraction, particle diameter and particle number density were deemed necessary and sufficient to characterize the soot at any spatial location. These measurements were performed simultaneously using a laser light scattering and extinction technique on a 0.5 mm horizontal by 5 mm vertical grid (same as temperature and TPD).

3.5.1 Scattering and Extinction Optical Train

A schematic of the laser light scattering and extinction optical train is shown in Figure 3.11. A Lexel Argon Ion laser operating on the green, 514.5 nm, line at a power of 0.4 Watts was used as the light source for scattering and extinction measurements. The

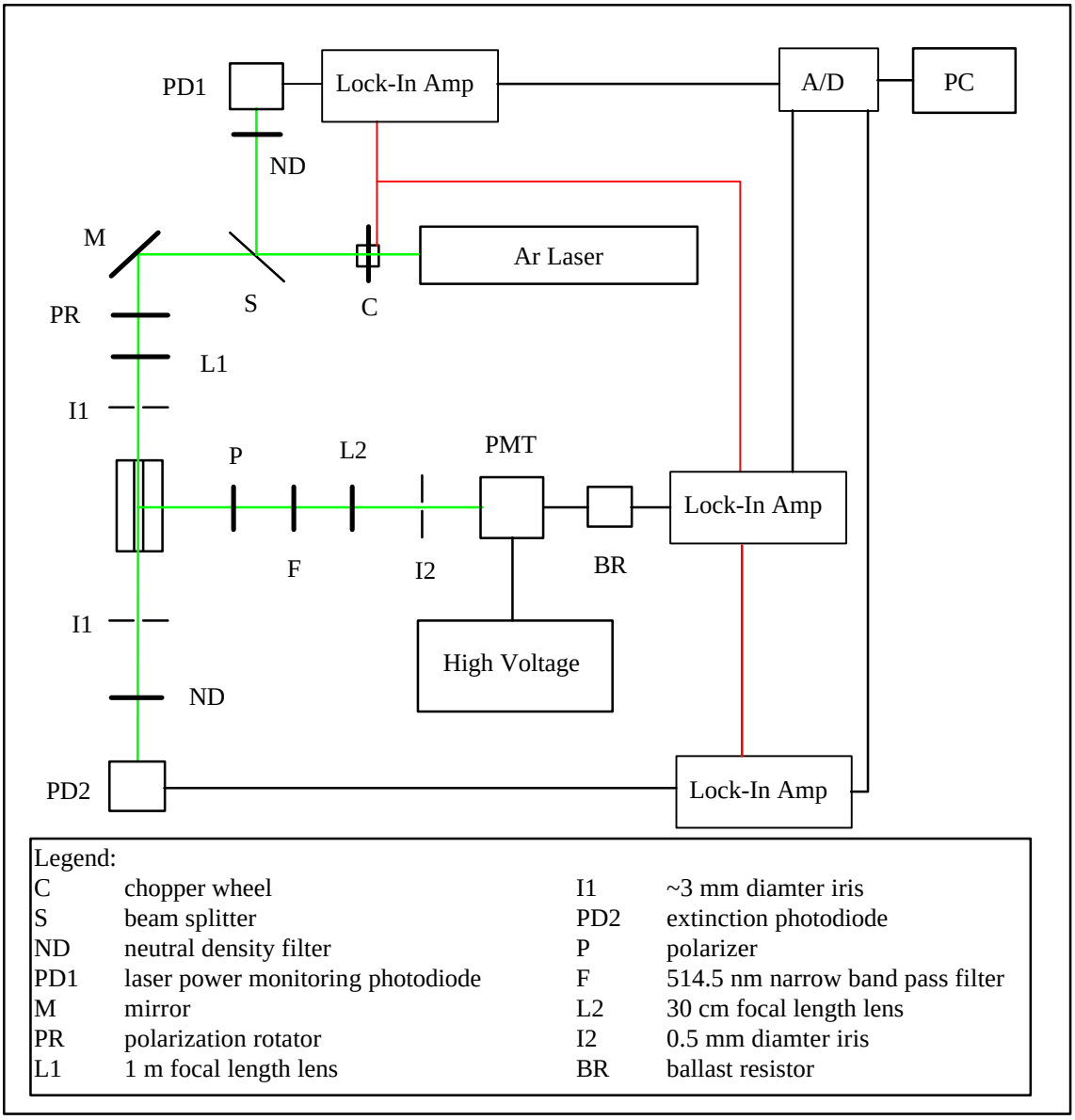

Figure 3.11 Scattering and Extinction Optical Train

laser power supply did not have an operational light stabilized mode so the laser was operated in constant current mode. Laser output power was adjusted using a portable laser power meter. Monitoring the laser power incident on a photodiode over the course of several hours revealed variations less than 0.5%. Nevertheless approximately 5% of the

laser output was split to a photodiode dedicated to monitoring laser power during experiments also showing negligible variations.

The laser beam was chopped at 400 Hz before being split to the power monitoring photodiode and steered toward the burner with two mirrors providing horizontal and vertical degrees of freedom for beam steering. An electrical square wave signal generated by the chopper wheel driver at the chopping frequency was used to trigger the lock-in amplifiers. The laser beam was aligned parallel to the burner slots and exit plane by adjusting the beam angles so that the beam uniformly grazed the burner slot partitions.

The scattering beam path polarizer was visually adjusted to the vertically polarizing orientation using the manufacturer's marks on the filter. The polarization rotator was adjusted by maximizing the output signal of the photomultiplier tube (PMT) collecting scattered laser light from propane gas.

A very long focal length lens, 1m, was chosen for L1 to provide a mildly converging and diverging beam waist and therefore virtually uniform beam diameter through the burner test section. Although the exact laser beam waist diameter was never measured, rough indications (burning holes in paper) showed that it was on the order of 1 mm or less. With the beam aligned parallel to the burner a piece of paper with cross-hairs drawn on it was placed concentric with the beam spot and the lens L1 was positioned as not to disturb the beam alignment with the cross-hairs.

The PMT inlet iris, I2, was coarsely adjusted to 60 cm separation with the laser beam using a tape measure. By splitting the I2 / laser beam separation distance with a 30 cm focal length lens ensured unity magnification in imaging the beam onto the iris. Fine

adjustment of the I2 / laser beam separation distance was performed by minimizing the projection diameter of scattering from a pin tip onto the iris plane. Final PMT / I2 alignment was accomplished by maximizing the PMT output signal collecting laser beam scattering from propane gas. A narrow band-pass 514.5 nm filter was placed in the scattering beam path to minimize the broad-band flame luminosity collected by the PMT.

Photomultiplier tubes are current (not voltage) transducers requiring a high voltage power source which determines the gain of the instrument. Higher voltages (as much as 2000 V) provide more gain but can also drive the PMT to behave nonlinearly with respect to its electrical current output / incident light sensitivity. Since the lock-in amplifier could only measure voltage, the current from the PMT was converted to a voltage across a ballast resistor. Similar to the high voltage gain, higher ballast resistor values create larger voltage signals but can introduce more “noise antenna” effects and require larger time constants on the lock-in amplifier slowing the PMT’s response. Using neutral density filters to check the output / input linearity and an oscilloscope to gauge signal noise, high voltage excitation of 595 V and a ballast resistor value of 1440 Ω were determined to be optimum.

Laser light on both the scattering and extinction beam paths were passed through the burner test section through 1/8 inch thick borosilicate glass windows. Window cleanliness prevented optical experiments from running more than ~1 hour. Running longer caused beam extinction through the windows to exceed 5% of the clean transmitted power.

3.5.2 Interaction of Light with Particles

A beam of light incident on an aerosol of particles, as found in the sooting regions of non-premixed flames, may be scattered, absorbed or transmitted. The amount of incident light not transmitted due to the combination of scattering and absorption is referred to as the beam extinction. The amount of beam extinction is a function of the optical properties of the particles as well as the size and particle number density of the particles.

Lorentz-Mie theory provides an analytical basis for predicting the interaction of electromagnetic radiation with solitary solid objects [Bohren, 1983 and Kerker, 1969] of which closed form solutions are readily available for spheres. Extrapolation of the single particle Lorentz-Mie solutions to dispersions of particles, such as soot aerosols in flames, may be done effectively if three conditions are met [Vandsburger, 1986]:

1. Separation distances between particles must be large enough that there is little electromagnetic interaction among them yielding particles that scatter as separate entities.

2. Multiple scattering is minimized by the dispersion of particles being very thin.

3. Particle number densities are sufficiently large and particle motions are sufficiently random that scattering from all of the individual particles yields a diffuse field obeying linear superpostion.

Vandsburger [1986] showed that typical soot aerosols fulfill all of the above requirements for application of Lorentz-Mie theory.

A special case of Lorentz-Mie theory, called Rayleigh theory, exists for particles whose diameters are much smaller than the wavelength of the incident light. Rigorously stated, Rayleigh theory is valid for the condition that

$$\alpha = \pi d/\lambda < 0.3 \qquad \textbf{Equation 3.1}$$

For particles in the Rayleigh limit one can safely neglect scattering as a source of laser beam extinction and assume that all extinction results from particle absorption. This simplifying assumption reduces the complex Lorentz-Mie spherical harmonics solution to simple linear algebraic equations.

For the 514.5 nm laser used for this study Rayleigh theory is strictly satisfied only for particles smaller than 50 nm; soot particles diameters over 100 nm were anticipated. Santoro *et. al*. [1983] showed that Rayleigh and Mie analysis of scattering and extinction measurements, using 514.5 nm wavelength light, only differ by about 10% for 100 nm soot particles and 25% for 120 nm particles and concluded that

> "Considering the uncertainties introduced through the choice of the index of refraction and particle size distribution function, use of Mie scattering theory with its added computational difficulties did not seem warranted…"

Considering the purpose of this study was mainly to *compare* varying degrees of dual mode combustion it was decided to compromise the better accuracy of Mie analysis for the convenience of Rayleigh analysis.

3.5.3 Extinction Measurement and Analysis

In the Rayleigh limit soot volume fraction, ϕ, may be calculated as

$$\phi = \frac{\lambda k_{ext}}{6\pi \cdot E(\tilde{m})} \qquad \textbf{Equation 3.2}$$

where $\lambda \equiv$ wavelength of incident light
$k_{ext} \equiv$ beam path extinction coefficient

and

$$E(\tilde{m}) = -\,\mathrm{Im}\left(\frac{\tilde{m}^2 - 1}{\tilde{m}^2 + 2}\right) \qquad \textbf{Equation 3.3}$$

where $\tilde{m} = (n - ki) \equiv$ soot particle complex index of refraction

Many investigators, including Dalzell and Sarofim [1969], Tien and Lee [1981] (review) and Chippett and Gray [1978], have reported values of soot complex index of refraction, $\tilde{m}$. For ease of comparison the most widely used value of $\tilde{m}$=1.57 - 0.56i [Smyth and Shaddix, 1996] was used for this study yielding a value of E(1.57 - 0.56i) = 0.2617 from Equation 3.3.

The beam path extinction coefficient, k_{ext}, for a beam traveling through a slab of length, L, is determined from the Lambert-Beer law as

$$k_{ext} = -\frac{1}{L}\ln\left(\frac{I}{I_0}\right) \qquad \textbf{Equation 3.4}$$

where $I \equiv$ transmitted beam intensity
$I_0 \equiv$ incident beam intensity

Extinction path lengths were measured as a function of height from PMT scattering signals by traversing the burner parallel to the incident beam with the laser beam passing through the sooting region (see Figure 3.11). The value of incident intensity, I_0, was measured

through the windows outside the flame. Linearity of the extinction photodiode was verified using neutral density filters of known absorption allowing output voltages to be used in Equation 3.4 instead of calibrated intensity measurements.

3.5.4 Scattering Measurement and Analysis

Equations used to calculate soot particle diameters and particle number densities require that scattering measurements made in arbitrary PMT ballast resistor voltage units, V_{exp}, be converted to volumetric scattering cross sections, Q_{VV}, with units of $\{m^{-1}\ str^{-1}\}$. The subscript "VV" indicates that the vertically polarized component of scattered light resulting from strictly vertically polarized incident light was measured. To do this, all scattering intensities measured with the PMT were scaled against a value for scattering from propane gas at STP determined in a calibration procedure before *each* test. Before the flame was lit and with all windows installed the PMT output voltage, $V_{cal,C3H8}$, in response to laser light scattering from propane gas issuing from the fuel slot of the burner was measured and recorded. The scattering intensity from propane was so much smaller than that from soot that the lock-in amp sensitivity for calibration, S_{cal}, had to be increased to 500 μV from the experimental run value, S_{exp}, of 200 mV and scaled later in the Q_{VV} calculation. Using the scattering calibration data and correcting for optical extinction along the extinction and scattering beam paths Q_{VV} may be calculated as [Vandsburger, 1986]

$$Q_{VV} = NC_{VV} = V_{exp}\left(\frac{C_{VV,C3H8} \cdot N_{C3H8}}{V_{cal,C3H8}}\right)\left(\frac{S_{exp}}{S_{cal}}\right)\left(\frac{1}{I_1/I_0 \cdot I_2/I_1}\right) \quad \textbf{Equation 3.5}$$

where N_{C3H8} ≡ number of propane molecules per unit volume, 2.4376×10^{19} molecules/cc for ideal gas behavior

$C_{VV,C3H8}$ ≡ propane differential scattering cross section, 1.21×10^{-30} m^2 str^{-1} [Kent and Wagner, 1982]

As a check for parasitic light corrupting the scattering calibration the ratio of propane scattering intensity to nitrogen scattering intensity was checked against the corresponding differential scattering cross section ratio reported by Kent and Wagner [1982] as 13.6. Variations of less than 4% from the published value were typical and deemed satisfactory being similar to the repeatability reported by Kent and Wagner [1982] of 5%. All scattering signal voltages from the PMT were corrected for "dark current" using scattering from helium as the datum for zero scattering.

The ratio I_1/I_0 is introduced into Equation 3.5 to correct for extinction of the incident beam before hitting the scattering volume and the ratio I_2/I_1 to correct for extinction of the scattered light between the scattering volume and the PMT as shown schematically in Figure 3.12. These two intensity ratios are calculated from previously measured extinction coefficients $k_{ext,ij}$ (for measurement grid height, j, and transverse location, i) as

$$I_1/I_0 = \exp\left(-\ k_{ext,i} \cdot \frac{L}{2}\right) \qquad \textbf{Equation 3.6}$$

$$I_2/I_1 = \prod_{i}^{n} \exp\left[-\ k_{ext,i} \cdot \Delta y\right] \qquad \textbf{Equation 3.7}$$

Choosing the sixth to third moment ratio, D_{63}, to be statistically representative of the soot paricle sizes [Santoro *et. al*. 1983]

$$D_{63} = \lambda\left(\frac{4}{\pi^2}\,\frac{E(\tilde{m})}{F(\tilde{m})}\,\frac{Q_{VV}}{k_{ext}}\right)^{1/3} \qquad \textbf{Equation 3.8}$$

where $$F(\tilde{m}) = \left|\frac{\tilde{m}^2 - 1}{\tilde{m}^2 + 2}\right|^2 \qquad \textbf{Equation 3.9}$$

$$F(1.57 - 0.56i) = 0.21502$$

and assuming the exponential approximation of the self-preserving soot particle size distribution function yields the soot particle number density, N.

$$N = \frac{12\phi}{\pi D_{63}^3} \qquad \textbf{Equation 3.10}$$

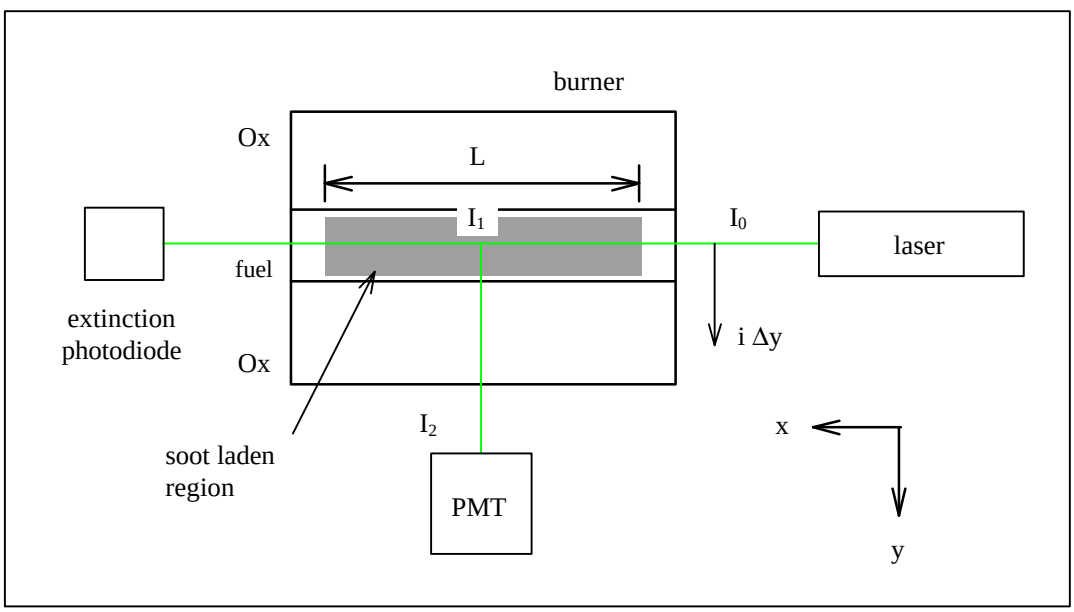

Figure 3.12 Beam Extinction Correction for Scattering Analysis

3.6 Velocity

Knowledge of the velocity fields in the flames studied was desirable for transforming measurements made in Eulerian (laboratory) coordinates into Lagrangian (particle tracking) coordinates and for calculating fluxes from concentration measurements. Velocity measurements were attempted using Particle Imaging Velocimetry (PIV) but spatially restricted flow seeding necessitated some velocity modeling to "fill in the gaps."

3.6.1 Particle Imaging Velocimetry

Adopting the "have burner…will travel" approach to combustion research, the Wolfhard-Parker burner was taken to the Buoyant Flames Facility at the National Institute of Standards and Technology in Gaithersburg, Maryland to perform Particle Imaging Velocimetry (PIV) measurements in the flames. The PIV technique is based on tracking flow seeding particles in Lagrangian coordinates in a two-dimensional plane. By tracking the change in position of a particle, $\Delta\vec{s}$, over a very short time period, Δt, one can estimate its instantaneous velocity vector, $\vec{v}$, as $\vec{v} \approx \Delta\vec{s} / \Delta t$.

A dual beam, frequency doubled, pulsed Nd:YAG laser operating on the 532 nm line was formed into a single vertical sheet and used to illuminate a two-dimensional plane perpendicular to and on center with the burner slots as shown in Figure 3.13. By capturing two flowfield images with a digital CCD camera on the order of 10μs - 100μs apart (depending on the magnitude of the velocities to be measured) an image cross correlation processor statistically identified particles and their change in position to yield

the velocity vector field in that plane. Not knowing the gas velocities ahead of time optimizing PIV timing was an iterative process.

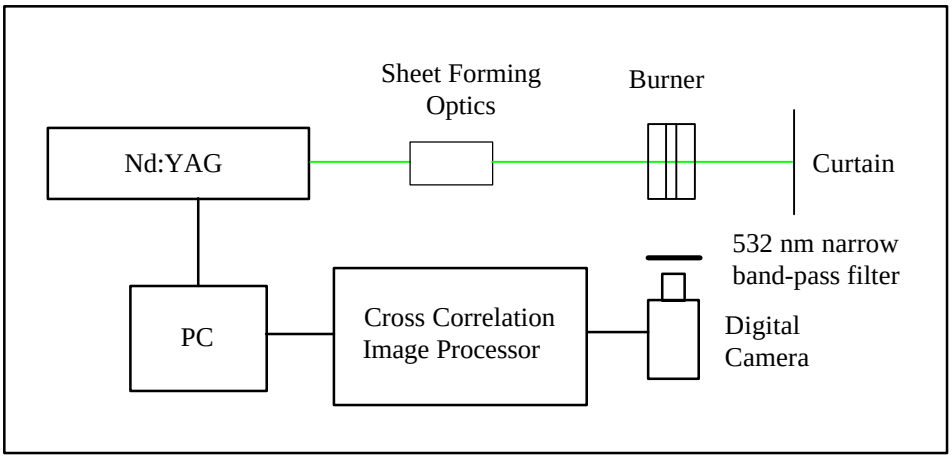

Figure 3.13 Schematic of Particle Imaging Velocimetry Facility

The flow was seeded with 0.5 μm Al_2O_3 particles introduced into the fuel slot and co-flow using a cyclone seeder. A 532 nm narrow band pass filter in front of the camera was required to reduce the broad band luminosity of the sooting region from masking the laser light scattering from the seed particles. Seeding of the oxidizer flow could not be achieved with this method because the seed would not have passed through the porous sinters. $TiCl_4$, as used by Kent and Wager [1981], could have been dissolved into the oxidizer flows which would form particles when coming into contact with water vapor in the combustion products. This seeding option was eliminated considering the extremely corrosive nature of $TiCl_4$ and safety issues associated with the toxic chlorine gas released by its reaction with water.

A PIV image of the seeded flow field in the single mode flame is shown in Figure 3.14. The image shows scattering from particles seeded into the center slot fuel flow and

the nitrogen coflow as well as scattering from the sooting region on the fuel side of the flame front. Figure 3.14 shows some dissymmetry between the coflow/oxidizer boundary streamlines most likely caused by uncertainty in the rotometer settings. Notice that the strong buoyant acceleration of the fuel flow combined with thermophoresis (Appendix A.3) causes a rapid tapering of the fuel flow seed.

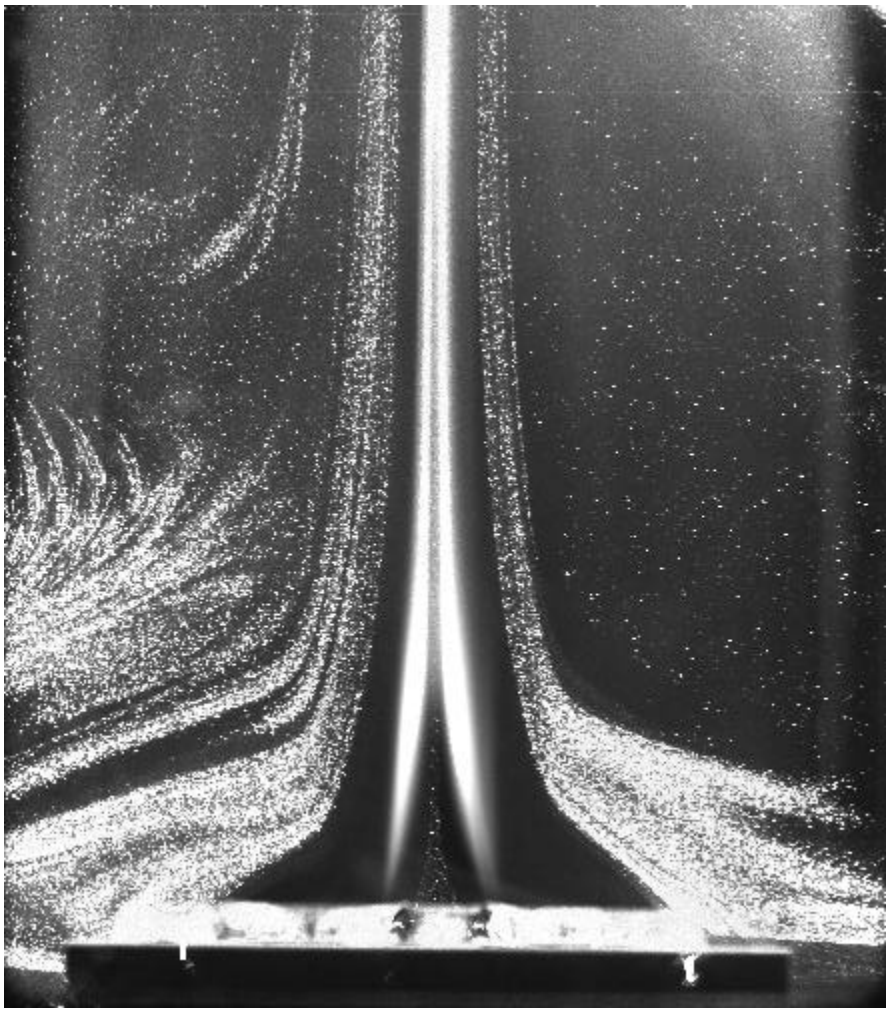

Figure 3.14 Single Mode Flame Flow Seeding

The absence of fuel slot born seed particles in the sooting region or at the flame front where hydrocarbon fuel must certainly exist is curious. With exception for

thermophoretic effects the seed particles were sufficiently small to accurately follow the gas *convective* streamlines. Absence of seed particles at the flame front supports the idea that the dominant mode of reactant transport to the flame front of this nonpremixed flame, commonly called a diffusion flame, is truly diffusion rather than convection. One might also argue based on this observation that the thermophoretic driving potential from the hot flame front toward the cooler centerline is stronger than the diffusion potential driving fuel from centerline to the flame front.

3.6.2 Velocity Calculations

Absence of seed particles in the sooting region and near the flame front prevented PIV measurements in those regions (Figure 3.14). This was especially unfortunate considering that velocity information in those areas were the most interesting and useful to this study. This section describes a simple velocity model used to estimate velocities in those regions where they could not be measured using PIV.

The convective streamlines bounding the fuel, oxidizer and coflow in the flame appear to be well approximated by the spatial extent of seed particles. However, transport processes such as mass diffusion across streamlines and thermophoretic acceleration of seed particles prevent the seed boundaries in the PIV images from being true streamlines. If stream tubes could be defined in the unseeded region which accurately interpolate the apparent streamlines the unmeasured velocity field could be calculated with a conservation of mass approach using temperature measurements to define the density field and a top-hat inlet velocity profile assumption.

If the flow under consideration were isothermal, interpolation of the apparent streamlines could be easily accomplished using an inviscid, incompressible conservation of energy approach such as the Bernoulli equation. Volumetric heat release from chemical reactions and work done on the fluid via non-negligible buoyant body forces prevent such a simple approach. Truly accurate modeling of the unseeded flow field with the apparent boundary conditions would require abandoning the simplicity of the streamtube calculation methodology in favor of full discretization of the Navier-Stokes equations. It was decided that such a modeling effort would be beyond the scope of this work.

Using the previously mentioned stream tube approach with the assumption that streamtube widths interpolate linearly at any given height (i.e. uniform width streamtubes) was used to *estimate* the unmeasured velocities as shown in Figure 3.15. Using images of a scale placed in the plane of the laser sheet, captured with the digital camera before each test, the width of the particle-free oxidizer flow could be measured from PIV images such as Figure 3.14 as a function of height. Optically measured extinction pathlengths were used to approximate "necking" of stream tube area parallel to the burner slots as a function of height above the burner.

A top-hat velocity profile at the inlet of the unseeded region was assumed by evenly distributing the oxidizer mass flow evenly among the 50 stream tubes used in the calculation. By conservation of mass along the jth stream tube at the ith elevation above the burner the velocity, v, was calculated as

$$\left\|\vec{v}_{i,j}\right\| = \frac{\dot{m}_{total}}{n} \frac{1}{\rho_{i,j}\left(\frac{w_i}{n} \cdot d_i\right)}$$ **Equation 3.11**

where $\dot{m}_{total}$ = total oxidizer mass flow from one slot

n = total number of stream tubes

w_i = width of unseeded region as measured from PIV image

d_i = stream tube depth approximated as optical extinction path length

$\rho_{i,j}$ = fluid density

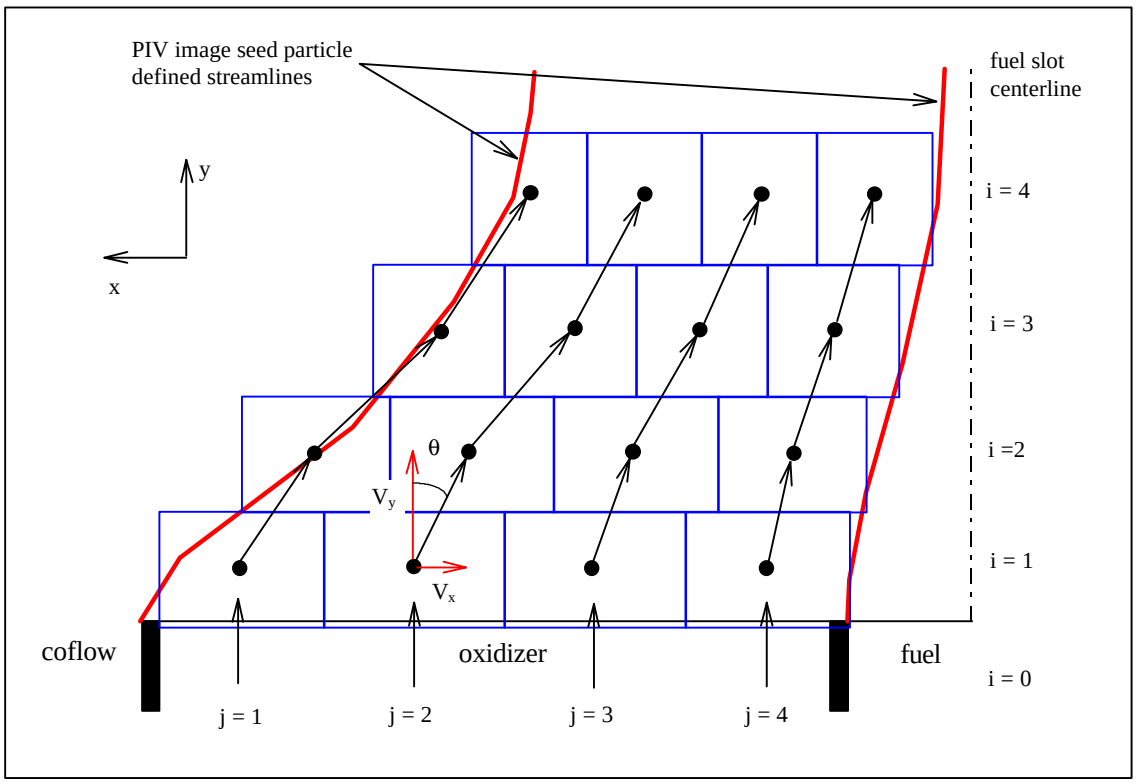

Figure 3.15 Velocity Model Grid Scheme

Fluid density was calculated as an ideal gas at atmospheric pressure, p_{atm}, and measured gas temperature, $T_{i,j}$, as

$$\rho_{i,j} = \frac{p_{atm}}{T_{i,j}} \frac{R_u}{MW_{gas}} \qquad \textbf{Equation 3.12}$$

The fluid was assumed to have a molecular weight, MW_{gas}**,** of 28 kg/kmol which is a fair assumption considering the molecular weights of typical oxidizers and diffusion flame combustion products range from 26 to 29 kg/kmol and ethylene's molecular weight of 28 kg / kmol.

Vertical and horizontal components of the resultant vector magnitude calculated in Equation 3.11 were determined from the relative locations of the ith and (i^{th} + 1) elevations of the jth stream tube (see Figure 3.15) as

$$\left\|\vec{v}_y\right\| = \left\|\vec{v}\right\| \cos\theta \qquad \textbf{Equation 3.13}$$

$$\left\|\vec{v}_x\right\| = \left\|\vec{v}\right\| \sin\theta \qquad \textbf{Equation 3.14}$$

Notice that the gas temperature is required to compute gas velocity and from the discussion in Appendix A gas velocity is required to calculate gas temperatures from thermocouple measurements. An iterative procedure was used where

- the measured thermocouple temperature used as an initial guess for gas temperature
- temperature guess was used to calculate gas velocity
- gas velocity was used to characterize the convection around the thermocouple junction for performing a radiation correction
- the corrected temperature is used as the next gas temperature guess with continued iterations until convergence criterion was met

The convergence criterion used for this calculation was based on the consecutive iteration magnitudes of the radiation correction as

$$\left| \sqrt{\sum_{i,j} \left(T_{gas} - T_{TC} \right)^2}_{current} - \sqrt{\sum_{i,j} \left(T_{gas} - T_{TC} \right)^2}_{previous} \right| < 0.01 \qquad \textbf{Equation 3.15}$$

Typically only four iterations were required to satisfy this convergence criterion.